metals

MDPI

Article

Acetic Acid Etching of Mg-xGd Alloys

Marcjanna Maria Gawlik [1,*], Björn Wiese [1], Alexander Welle [2], Jorge González [1], Valérie Desharnais [1,3], Jochen Harmuth [1], Thomas Ebel [1] and Regine Willumeit-Römer [1]

1 Helmholtz-Zentrum Geesthacht, Institute of Materials Research, 21502 Geesthacht, Germany; bjoern.wiese@hzg.de (B.W.); jorge.gonzalez@hzg.de (J.G.); valerie.desharnais@sympatico.ca (V.D.); jochen.harmuth@hzg.de (J.H.); thomas.ebel@hzg.de (T.E.); regine.willumeit@hzg.de (R.W.-R.)

2 Karlsruhe Institute of Technology (KIT), Institute of Functional Interfaces, Karlsruhe Nano Micro Facility, 76344 Eggenstein-Leopoldshafen, Germany; alexander.welle@kit.edu

3 School of Computer Science, McGill University, Montréal, QC H3A 2T5, Canada

* Correspondence: marcjanna.gawlik@hzg.de; Tel.: +49-4152-87-1917

Received: 14 December 2018; Accepted: 21 January 2019; Published: 23 January 2019

Abstract: Mg-*x*Gd alloys show potential to be used for degradable implants. As rare earth containing alloys, they are also of special interest for wrought products. All applications from medical to engineering uses require a low and controlled degradation or corrosion rate without pitting. Impurities from fabrication or machining, like Fe inclusions, encourage pitting, which inhibits uniform material degradation. This work investigates a suitable etching method to remove surface contamination and to understand the influence of etching on surface morphology. Acetic acid (HAc) etching as chemical surface treatment has been used to remove contamination from the surface. Extruded Mg-*x*Gd (x = 2, 5 and 10) discs were etched with 250 g/L HAc solution in a volume of 5 mL or 10 mL for different times. The microstructure in the near surface region was characterized. Surface characterization was done by SEM, EDS, interferometry, and ToF-SIMS (time-of-flight secondary ion mass spectrometry) analysis. Different etching kinetics were observed due to microstructure and the volume of etching solution. Gd rich particles and higher etching temperatures due to smaller etchant volumes promote the formation of pits. Removal of 2–9 µm of material from the surface was sufficient to remove surface Fe contamination and to result in a plain surface morphology.

Keywords: Mg-Gd alloy; surface treatments; acetic acid etching; surface characterization

1. Introduction

The use of Mg alloys as biocompatible and degradable materials has been described as innovative research field [1–4]. Mg alloys have stimulating effects on osseointegration and osteoconduction [5–7]. Additionally, Mg can efficiently be alloyed with elements that are non-toxic to the human body [8,9]. For load-bearing implants that are used in fracture fixation, Mg alloys have Young's moduli closer to those of human bone [10], unlike Ti alloys, steels and most of the other medical alloys. Mg alloys with rare earth additions have been gaining importance in the field of degradable Mg alloys [11]. For biocompatible Mg alloys, the highly soluble elements Dy and Gd are advantageous due to the possibility of avoiding the formation of secondary phases [12]. Rare earth secondary phases with high electrochemical differences to Mg provoke localized galvanic corrosion [13–18]. In Mg alloys with rare earth additions of Gd, Dy, and Nd, for example, rectangular hydrides were found within the material. Rare earths have a higher affinity to H_2 compared to Mg and will form rare earth hydrides in the presence of water or hydrogen. Hence the formation of GdH_2 in Mg occurs rather easily [19]. These hydrides are reported to form in the material via different pathways during fabrication and preparation [11,19–21]. Mg-Gd and Mg-Dy alloys are already under investigation [11,22–26]. Gd plays no role in human metabolism. However, Feyerabend et al. [9] performed an in vitro study

of cytotoxicity and inflammatory response and found the best cytocompatible rare earth alloying additions to be Dy and Gd. Mg-10Gd typically had the slowest material degradation rate, as reported in a study that investigated Mg-2Gd, Mg-5Gd, Mg-10Gd, and Mg-15Gd alloys [11]. In vivo studies showed good healing and bone implant integration, when investigating the degradation behavior of Mg-Gd alloys [27–29].

Acid etching as surface treatment is used to remove galvanic corrosion inducing impurities like Fe and processing deformation from the surface [30–33]. Fe impurities have to be removed from the surface to avoid galvanic corrosion [34]. Deformation from machining change, e.g. grain size, defect density and internal stress in the subsurface [30,35,36], which has a direct influence on mechanical properties and corrosion resistance [37–40]. Most of the studies on etching were performed on AZ alloys, which are reported not to be suitable in biodegrading environments due to the Al content. The neurotoxicity of Al has been discussed and is thought to increase the risk of Alzheimer's disease [41–44]. Thus introducing Al in the human body via AZ based implants should be avoided. To date, etching Al-free Mg alloys have been rarely studied. However, the studies on AZ alloys are a good basis for the development of suitable etching treatments for biocompatible Al-free Mg alloys and Mg-RE alloys in bio-structural applications. The advantage of acid etching on Mg-5Gd alloys has been demonstrated by in vitro degradation testing [45].

Nwaogu et al. [31,32] used organic (acetic acid, oxalic acid, citric acid) and inorganic acids (sulfuric acid, nitric acid, phosphoric acid) to clean AZ31 sheets of impurities such as Fe and Ni. A greater amount of material was removed as the etching time was increased, which led to more impurities being removed. The greatest layer thickness removed from the surface layer was 20 µm. Acetic acid etching showed the highest degradation resistance as tested by electrochemical impedance spectroscopy (EIS) and salt spray in 5 wt.% NaCl [31]. Gray-Munro et al. [33] studied acid etching (90% H_3PO_4) on AZ31 foils as a pretreatment for calcium, phosphate, and polymer coatings. After etching, the passive surface oxide layer was thicker compared to that of the as-received condition. The surface morphology was also more uniform as post-production marks were removed by etching [33]. Song and Xu [30] studied sulfuric acid etching (10% H_2SO_4 for 20 s) on AZ31 sheets. By etching the surface, Fe impurities and the deformed surface layer that resulted from sandblasting were removed. Compared to the as-received and heat-treated conditions, etching increases the degradation resistance as measured by mass loss, hydrogen evolution, potentiodynamic polarisation (PDP) and EIS [30]. Supplit et al. [46] used acetic, nitric, phosphoric, and hydrofluoric acid etching solutions to decrease the degradation rate of AZ31 sheets. They achieved a decrease in the degradation rate by a factor of 60 on testing in 5 wt.% NaCl and measured by hydrogen evolution. They used a combination of acetic acid as a pretreatment and a sol-gel coating afterwards. Phosphoric acid was the second most effective acid in this experiment, while hydrofluoric acid etching resulted in the fastest degradation of testing in 5 wt.% NaCl [46].

Thus, etching is a potential way to remove impurities and deformed material from the surface, however, the wrong choice of etching agent and processing parameters can lead to undesirable degradation effects or an unnecessary loss of bulk material. The current work aims to understand which parameters of the etching process affect material degradation and to find a suitable etching treatment for Mg-*x*Gd alloys using acetic acid. The etching treatment has to uniformly remove material without localized etching pits, and also eliminate harmful contaminants from the fabrication process. The positive influence of HAc etching on the degradation rate of Mg-5Gd has been presented in a previous study [45].

2. Materials and Methods

2.1. Material Casting and Processing

Three different Mg-Gd alloys were used in this study. Melting was performed using an Ar + 3 vol.% SF_6 shielding gas in an induction furnace, (Nabertherm GmbH, Lilienthal, Germany). Gd was added to a Mg melt that was held at 710 °C. The alloys produced had 2, 5, and 10 wt.% Gd

additions. The alloys were cast into preheated molds at 550 °C. The cast ingots were then solution heat treated at 515 °C for 6 h and then processed by indirect extrusion (ratio 1:25) at a temperature of 400 °C and extrusion ram speed of 2 mm/s. The resulting extrusions had round profiles with a 10 mm diameter. A more detailed description is published in Harmuth et al. [47]. The round extruded rods were machined to a diameter of 9 mm, and then milled and cut into discs with a height of 1.5 mm (Figure 1). This initial state will be referred to the as as-received (AR) condition. Atomic absorption spectroscopy (AAS) measurements were performed in [47] to compare the Fe amount of AR bulk material for Mg-2Gd (Fe 20 ppm), Mg-5Gd (Fe 49 ppm), and Mg-10Gd (Fe 119 ppm).

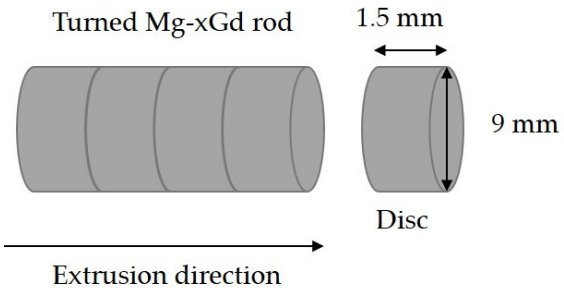

Figure 1. Charting of an extruded Mg-*x*Gd rod after machining to a diameter of 9 mm. Discs in cylindrical form with a diameter of 9 mm and a height of 1.5 mm were cut off by milling.

2.2. Etching Procedure

Before etching, the density and weight of the samples were determined (using an electronic balance "RADWAG MYA 2.4 Y" (RADWAG, Radom, Poland) with an accuracy of 0.01 mg) and measured (using calipers with an accuracy of 0.01 mm). The discs were ultrasonically cleaned in 3 mL n-hexane for 40 min to remove organic contaminants, subsequently dried for 30 min in a fume cupboard and re-weighed. The etching solution was prepared using double distilled water and acetic acid (HAc) (J.T. Baker, Avantor Performance Materials, Inc, Center Valley, PA, USA). Etching of the samples, shown in Figure 1, was performed in 5 mL or 10 mL of HAc etchant solution, corresponding to 2.9 or 5.9 mL/cm^2. The concentration of HAc was chosen after a previous study of Gawlik et al. [45]. Acid etching was performed by first pouring 250 g/L HAc solution into a watch glass. Cleaned samples were dipped for one second into the solution, flipped over and then re-submerged in the solution for a certain time varying between 15 s and 150 s. To stop the reaction, the samples were first immersed in 40 mL of 1 mol/L NaOH for 30 s, then into 40 mL of double distilled water for 30 s and finally into 40 mL of acetone for 30 s. The samples were then dried using a lint-free tissue. Finally, the samples were again ultrasonically cleaned in 3 mL of n-hexane for 40 min.

2.3. Determination of Material Removal

Etching was performed for 15 s in 5 mL, 150 s in 5 mL, and 150 s in 10 mL of the HAc solution. Six samples of each alloy were etched for each condition and the mean and standard deviation of removed material was calculated. For every etched sample, the material removal M in µm normalized to the surface area was calculated by the following formula:

$$M = \frac{\Delta m}{\rho \cdot A} \cdot 10^4 \quad (1)$$

where Δm is the mass loss in g as measured by the difference in mass before and after HAc etching, ρ is the alloy density in g/cm^3 and A is the disc surface area in cm^2.

2.4. Determination of the Temperature and pH

Before etching, the pH of the HAc solution was measured with a miniFET pH probe (Sentron Europe BV, VD Leek, The Netherlands) with an accuracy of 0.01. A thermocouple (MT2/ST) (otom

Group GmbH, Bräunlingen, Germany) was used to measure the initial and final temperatures of each sample during etching. This was done by applying a thermocouple immediately onto the sample surface after flipping over for the full duration of the etching. An additional three samples of each Mg-*x*Gd alloy were etched in 5 mL and 10 mL of 250 g/L HAc for 15 s, 120 s, and 150 s. Only one additional sample was etched in 5 mL and 10 mL per duration of 30 s, 60 s, and 90 s. After etching of the samples was complete, 200 µL of the remaining HAc solution was used to measure the pH. The pH was measured for solutions after 15 s etching in 5 mL and 150 s etching in 5 mL and 10 mL. Mean value and standard deviation of three samples and solutions were calculated for temperature (15 s, 120 s, and 150 s) and pH difference.

2.5. Interferometry

White light interferometry (WLI), performed with a non-contact interferometer (Contour GT-K, Bruker Corporation, Billerica, MA, USA) was used to analyze the topography after etching. The data from these measurements were analyzed using "Vision64" software (version 5.41 update 1, Bruker Corporation, Billerica, MA, USA). The raw data was fitted with an F-operator to correct the cylindrical form and tilt of the samples. A 3D Filter, "Mask Data" (Vision64 5.41 update 1, Bruker Corporation, Billerica, MA, USA), was then used to crop a circle with a diameter of 8 mm out of the data to avoid including the damaged edges arising from the machining process in the etching pit analysis. Peak-Valley difference and the surface roughness Sa (arithmetic mean of the absolute value of the height within sample area [48]) were determined with the 3D Analysis Tool "S Parameters-Height" (Vision64 5.41 update 1, Bruker Corporation, Billerica, MA, USA). Pits were then counted using the 3D Analysis Tool "Multiple Region" (Vision64 5.41 update 1, Bruker Corporation, Billerica, MA, USA) by searching for surface depressions with areas >800 μm^2 and depths greater than 15 µm below the mean surface height. These identification parameters were determined by a trial and error process of testing different values to find those capable of separating the valleys from the reference plane. Three samples from each of the etching conditions were measured to calculate the average and standard deviation for the number of pits per mm^2.

2.6. Micrographs

Micrographs were taken from cross-sections that were orientated parallel to the extrusion direction. The samples were embedded in methyl methacrylate (Demotec 30®, Demotec Demel e.K, Nidderau, Germany) and after hardening were ground with SiC papers of P320, P500, P800, P1200, and P2000 until half of the disc diameters. After grinding, a water-free 1 µm oxide polishing suspension solution (OPSTM, Cloeren Technology GmbH, Wegberg, Germany), 1 µm diamond solution and ethylene glycol were used for polishing. The embedded samples were immersed for a few seconds into a picric acid solution (VWR International, Radnor, PA, USA) to be able to observe the microstructure under a standard optical microscope (OM Leica DMI5000 M, Leica Microsystems GmbH, Wetzlar, Germany). Three micrographs per AR sample from each alloy were prepared. Two different sections were determined as they were either of a deformation zone (DZ) or a twinning zone (TZ) originating from the edge of the sample into the bulk material. The thicknesses of these zones were measured with the software "analySIS Pro" (version 5, Olympus Soft Imaging Solutions GmbH, Münster, Germany). Mean thickness value and standard deviation of the DZs and TZs were calculated from fifteen measurements per sample. One micrograph per etched (150 s in 5 mL) sample from each alloy was prepared to analyze the change in microstructure.

2.7. SEM and EDS

The surface of etched Mg-*x*Gd specimens was analyzed both parallel and perpendicular to the extrusion direction. Particle traces of cross sections, which were seen in the micrographs, were analyzed for one sample of Mg-10Gd with Energy-dispersive X-ray spectroscopy (EDS) (IXRF Sytems, Austin, TX, USA). The cross sections were prepared in the same way as described above. The morphology perpendicular to the extrusion direction was observed using the secondary electron

(SE) and backscattered electron (BSE) modes in a Tescan Vega III SB scanning electron microscope (TESCAN, Kohoutovice, Czech Republic) operating at 15 kV with a working distance of 15 mm. Particle element analysis was done using EDS and quantified using the "Iridium Ultra" (version 2.4 F, IXRF Sytems, Austin, TX, USA) software.

2.8. ToF-SIMS

ToF-SIMS (time-of-flight secondary ion mass spectrometry) was performed on a TOF.SIMS5 instrument (ION-TOF GmbH, Münster, Germany). This spectrometer is equipped with a Bi cluster primary ion source and a reflectron type time-of-flight analyzer (ION-TOF GmbH, Münster, Germany). Ultra-high vacuum base pressure was $<5 \times 10^{-9}$ mbar. For high mass resolution the Bi source was operated in "high current bunched" mode providing short Bi^+ primary ion pulses at 25 keV energy, a lateral resolution of approx. 4 µm, and a target current of approx. 1.5 pA at 14 kHz repetition rate. The short pulse length of 1.2 ns allowed for high mass resolution. Spectra were calibrated on the omnipresent $^{26}Mg^+$, $^{158}Gd^+$ and $GdMgO_2^+$ peaks, mass deviations were <10 ppm. For depth profiling a dual beam analysis was performed in non-interlaced mode: The primary ion source was operated in "high current bunched" mode with a scanned area of 500 × 500 µm^2 (3 frames with 128 × 128 data points) and a sputter gun (operated with O_2^+ ions, 1 keV, scanned over a concentric field of 750 × 750 µm^2, target current 200 nA, 45° angle of incidence) was applied to erode the sample for 6 s followed by a 0.3 s pause. Stable analysis conditions were ensured, for 6 subsequently performed depth profiles on two different Mg-2Gd samples the total Gd signal intensities varied less than 2.5% (mean value / standard deviation). To calibrate the depth scale for the dynamic SIMS (secondary ion mass spectrometry) experiments one polished specimen of each alloy was briefly precleaned with a low sputter ion dose density and subsequently eroded with a 1 keV oxygen beam in a 250 × 250 µm^2 crater with a controlled sputter ion dose density of 3×10^{18} 1/cm^2 ± 0.5%. During these erosions Mg and Gd signals were found to be constant from a depth of 25 nm onwards as soon as the sputter/oxygen implantation equilibrium was reached and a very thin non-metallic contamination layer was removed. Crater depths were measured by White light interferometry (WLI) (Contour GT-K, Bruker Corporation, Billerica, MA, USA). All alloys had eroded to a depth of 3.5 µm ± 10%. Based on these data a mean sputter yield of 5.02 was determined, being in good agreement with semi-empirical calculations from Yamamura et al. [49] indicating for pure Mg a sputter yield of 5.38.

In contrast to other surface analysis techniques, like X-Ray Photoelectron Spectroscopy, SIMS is semi-quantitative. Hence, absolute atom ratios can only be achieved by using external calibration standards and by taking the matrix effect into account. This effect is based on different sputter rates and different ionization yields for the elements to be studied in different matrices. Based on the known Mg/Gd ratios (Gd content varying from 2 to 10 wt.%, corresponding to 0.34 to 1.7 at.%) the linearity of the measured Gd^+ signal intensities obtained from depth profiles was good. With all instrument parameters held constant relative Gd^+ signal intensities of 1:2.5:4.5 were found for the Mg-2Gd, Mg-5Gd, and Mg-10Gd samples. This means that the investigated sample set showed no varying matrix effect for the different alloys, since Mg is the dominating matrix element with >98 to >99 at.%.

3. Results

3.1. Micrographs

Deformed grains and twins (see Figure 2a) were observed in the near surface region. Within DZ the grain structure was not visible. Inside TZ many twins (straight black lines inside of the grains) were observed. Additional particles were partly clustered and aligned in the extrusion direction. They are curved inside the DZ and TZ, this is a result of the milling process (see Figure 2b). The aligned particles are mainly clustered in Mg-10Gd, while all other alloys, show scattered distribution of particles and particle lines.

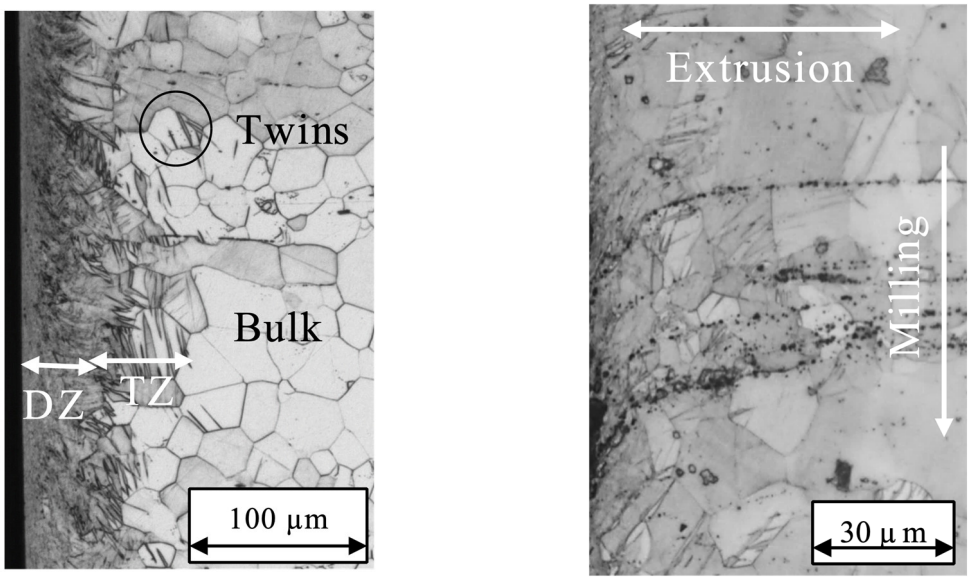

Figure 2. Micrographs of Mg-10Gd cross sections: (**a**) As received surface edge with deformed layer including a deformation zone (DZ) and twinning zone (TZ); (**b**) linear particle cluster are curved inside TZ.

After 150 s HAc etching in 5 mL solution, the surface edge in Figure 3 is more even with increasing Gd amount. The number of clustered particles is increasing with Gd amount. In Figure 3a, some single particles and lines are visible for Mg-2Gd, whereas Mg-10Gd in Figure 3c has accumulations of particle lines. With decreasing Gd amount the number of twins is increasing. For Mg-2Gd some deformed grains and a significant part of the TZ are still visible after the etching procedure. For Mg-5Gd the most of grains are deformation-free and some single twins are still visible. Mg-10Gd has a completely deformation-free surface edge.

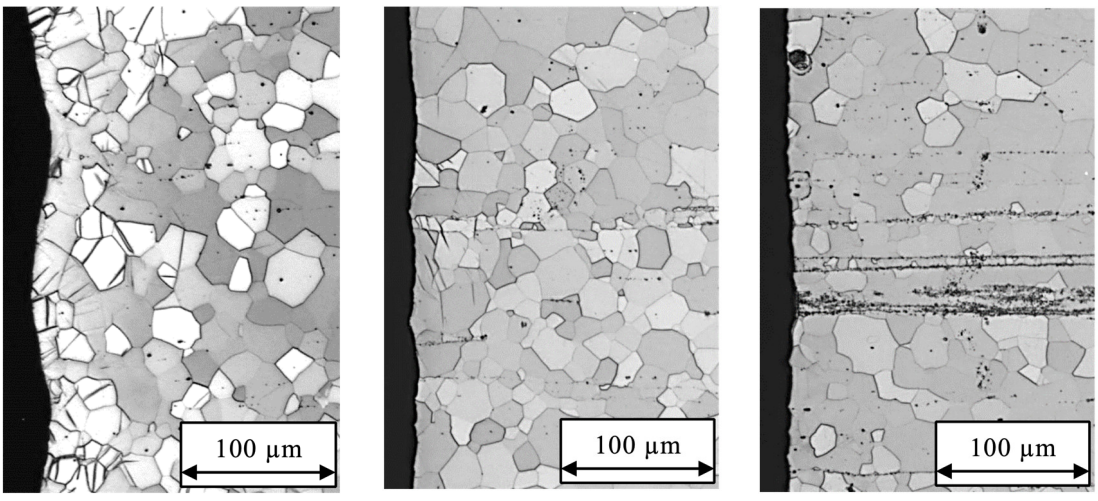

Figure 3. Micrographs cross sections after etching with 250 g/L for 150 s in 5 mL acetic acid (HAc) solution: (**a**) uneven surface edge of Mg-2Gd with partly non-deformed grains and grains including twins, some single black particles are visible; (**b**) mainly deformation free surface edge of Mg-5Gd with some single twins and partly visible particle lines; (**c**) deformation free surface edge of Mg-10Gd with linear particle cluster.

Within the standard deviation all alloys showed similar deformation zone (DZ) widths (Figure 4a), while mean value and standard deviation of TZ decreased with increasing Gd content. A high standard deviation of TZ arise from strong variation in twin depth for different positions, especially for Mg-2Gd. With increasing Gd amount the twin depth is shorter and more clustered.

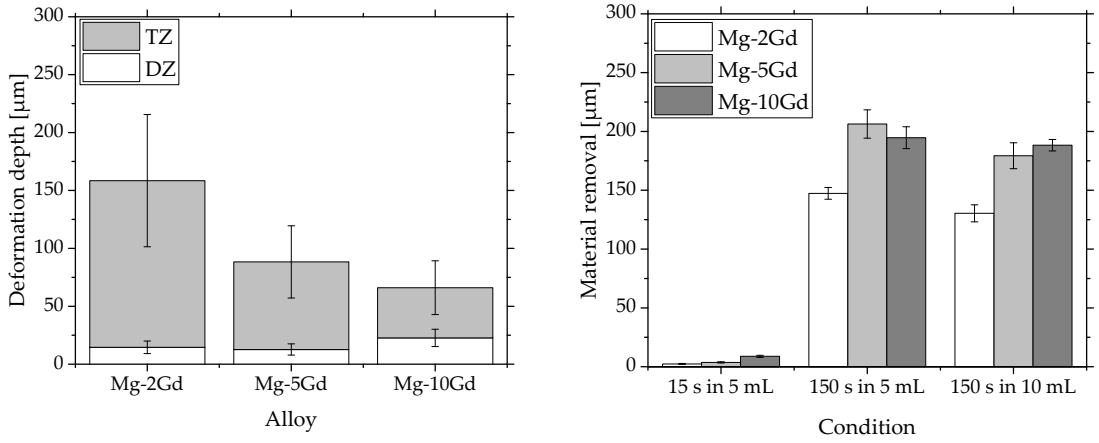

(**a**) (**b**)

Figure 4. Diagrams of: (**a**) Mean value and standard deviation of DZ and TZ calculated for fifteen different regions per sample. Three samples per alloy were measured; (**b**) mean value and standard deviation of six samples for the amount of material removed from the Mg-*x*Gd alloys after each etching treatment. The material removal increases with higher Gd content for all etching conditions. For each alloy the material removal after etching for 150 s in 5 mL and 10 mL solution are comparable.

3.2. Material Removal

Figure 4b and Table 1 indicate that basically more material is removed when the Gd content of the alloy is increased. After 15 s HAc etching, deformation and twins are still existing in all alloys. Using a longer etching time of 150 s, DZ is removed completely for all alloys and volumes. The calculations of material removal suggest a TZ free material for Mg-5Gd and Mg-10Gd for both etching volumes.

Table 1. Mean value of removed material and standard deviation of six samples for the Mg-*x*Gd alloys after each etching.

Condition	Mg-2Gd	Mg-5Gd	Mg-10Gd
M after 15 s in 5 mL [µm]	2.4 ± 0.4	3.6 ± 0.5	8.9 ± 0.9
M after 150 s in 5 mL [µm]	147.4 ± 5.0	206.3 ± 12.1	194.7 ± 9.4
M after 150 s in 10 mL [µm]	130.4 ± 7.2	179.3 ± 11.0	188.3 ± 4.9

3.3. SEM and EDX

Etching pits were observed for all alloys after 150 s etching in the 5 mL and 10 mL of 250 g/L HAc solutions. At the center of some deeper etching pits, Gd rich particles were detected (see Figure 5a,b with white spots). The Gd rich particles, identified by EDS, are either accumulated in a spot or clustered in lines. Next to Gd hydrides which were mentioned before, Kubásek and Vojtěch [50] found also oxides, which are assumed as Gd_2O_3 or $GdMg_2O_4$, formed during melting and casting. Hort et al. [11] ascertain a formation of Gd_2O_3 or $GdMg_2O_4$ during casting as well. Due to the small size of the particles it was not possible to determine the specific rectangular shape of hydrides. For this reason, it is not possible to distinguish between Gd oxides and hydrides and the mentioned particles are defined as Gd rich particles within this study.

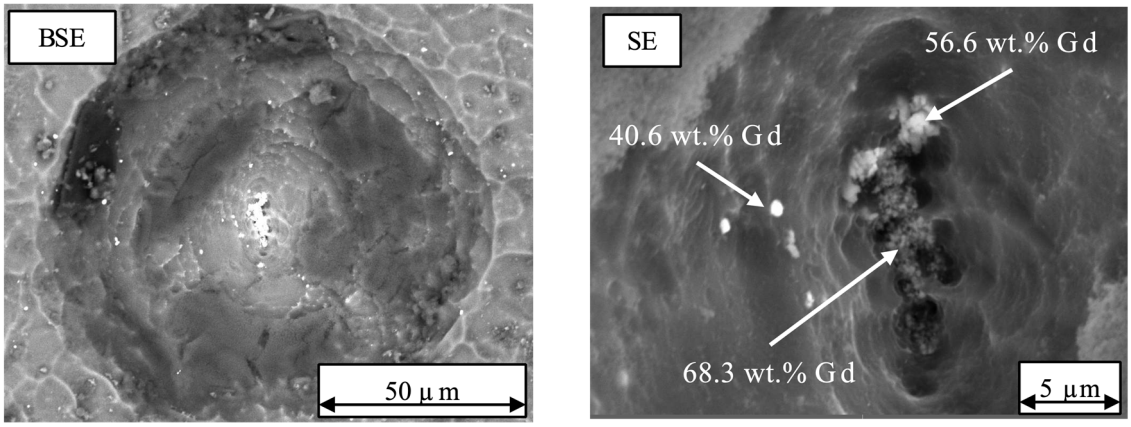

(**a**) (**b**)

Figure 5. SEM picture of one etching pit on the surface of the Mg-2Gd alloy after etching for 150 s in a 5 mL solution of 250 g/L HAc: (**a**) backscattered electron (BSE)-mode, formation of an etching pit inside the matrix with particles at the center; (**b**) secondary electron (SE) mode: higher magnification of accumulated Gd rich particles (white spots) at the center of an etching pit.

Using EDS it has been shown that the visible lines of particles are enriched with Gd (Table 2). In Figure 6 the corresponding points measured by EDS are marked. Inside the matrix at point 3, 9.7 wt.% Gd was measured, very similar to the nominal 10 wt.%. At the other positions marked 1 and 2, 62.8 wt.% and 30.5 wt.% of Gd was measured, respectively.

Table 2. EDS analysis from three spots shown in Figure 6.

Element	1	2	3
Mg [wt.%]	37.2	69.5	90.3
Gd [wt.%]	62.8	30.5	9.7

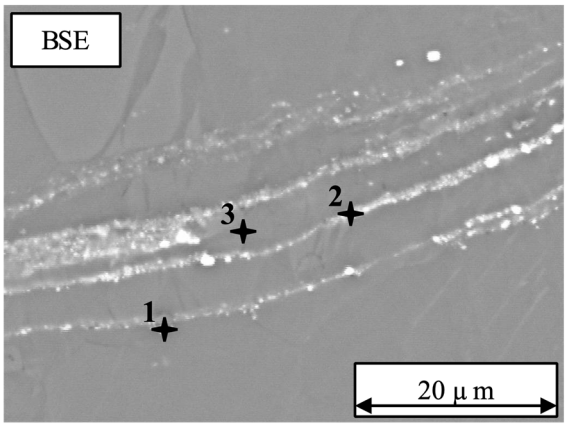

Figure 6. SEM micrograph obtained using the BSE mode of the as-received Mg-10Gd. Several lines of particles are curved inside the TZ and DZ of the Mg-10Gd material. EDS analysis was done at the three positions indicated to determine the Gd content.

3.4. Temperature and pH

Immersion in 5 mL for 15 s resulted in similar pH changes for all the Mg-*x*Gd alloys (see Table 3). After etching for 150 s the change in pH is higher for the 5 mL experiments compared to 10 mL experiments. In contrast to the 5 mL experiments, immersion in 10 mL shows that the change in pH is

increasing slightly with increasing Gd content. However, systematic errors in the pH measurement setup lead to the assumption, that pH changes for all alloys in 10 mL are comparable.

Table 3. Δ pH of HAc solution after etching the Mg-*x*Gd alloys in 5 and 10 mL solution.

Condition	Mg-2Gd	Mg-5Gd	Mg-10Gd
Δ pH after 15 s in 5 mL	0.07 ± 0.06	0.00 ± 0.00	0.20 ± 0.10
Δ pH after 150 s in 5 mL	1.47 ± 0.12	1.40 ± 0.00	1.47 ± 0.06
Δ pH after 150 s in 10 mL	0.73 ± 0.12	0. 83 ± 0.06	1.00 ± 0.00

Figure 7 indicates an increase in temperature with immersion time for all alloys and solution volumes. For the Mg-2Gd and Mg-5Gd alloys etched in 5 mL, the temperature rises linearly with time while the other conditions show a constant value of temperature change after around 120 s and longer. Additionally, the change of temperature is higher for etching in 5 mL compared to 10 mL.

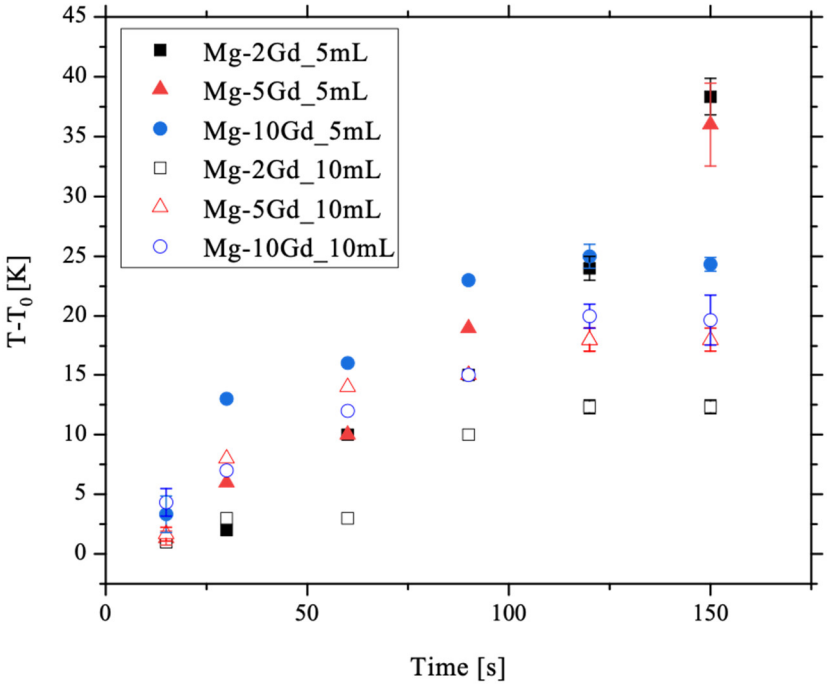

Figure 7. Diagram of T-T_0 plotted against time. T-T_0 increases with increasing time. Temperature increases are greater on etching in 5 mL compared to 10 mL solutions. Mean value and standard deviation of 3 samples were calculated for the time steps 15 s, 120 s, and 150 s.

3.5. Interferometry

Marks resulting from the machining with a wavelike structure were characteristic for the AR surface, as shown in Figure 8a. The color scale in Figure 8 shows the difference between the highest and lowest point of the surface for a Mg-2Gd specimen, as an example. After etching for 15 s in 5 mL the milling marks remained and no etching pits were formed (Figure 8b). However, the peak height as well as the difference in height of peak to valley are reduced. A slight decrease in Sa is also measurable after etching for 15 s compared to the AR condition. After etching for 150 s in 5 mL and 10 mL HAc solution, the surface morphology is very different compared to the AR surface as visible in Figure 9. The roughness Sa is higher after treatment in the 5 mL solution compared to 10 mL.

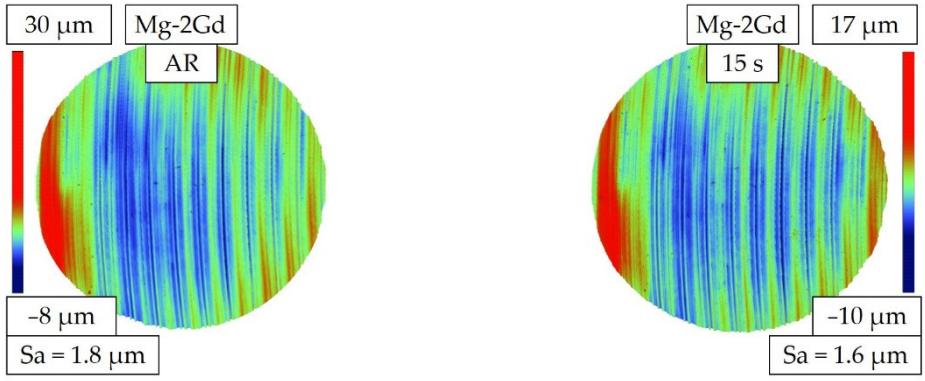

Figure 8. Topographies of the Mg-2Gd alloy as measured by white light interferometry (WLI): (**a**) Topography in as-received (AR) state with machining marks and a peak-valley difference of 38 (30 µm to −8 µm) (**b**) Topography after etching with 250 g/L HAc for 15 s in 5 mL of solution. Machining marks are still visible and the peak-valley difference of 27 µm (17 µm to −10 µm) is reduced in as compared to the AR state.

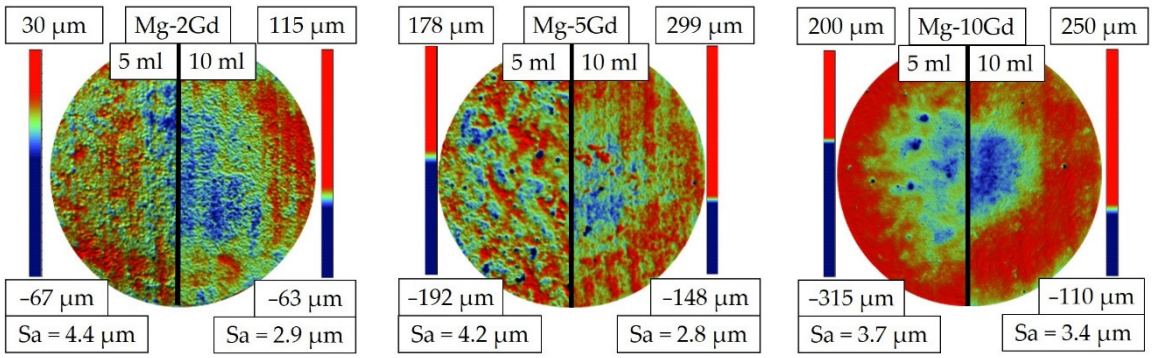

Figure 9. Topographies and their describing parameters of Mg-*x*Gd alloys measured using WLI after etching with 250 g/L HAc for 150 s; left half image: 5 mL, right half image: 10 mL etching volume, (**a**) topographies of Mg-2Gd; (**b**) topographies of Mg-5Gd; (**c**) topographies of Mg-10Gd.

Figure 9 compares the etching effect after 150 s for different Gd contents and two different volumes of etching solution each. The left half shows the result after etching in 5 mL, the right one in 10 mL solution. For the Mg-2Gd specimens (Figure 9a) the machining marks are much less obvious compared to the AR state (Figure 8a). Etching pits have been formed with etching in 5 mL leading to a higher number of pits/mm^2 (Table 4) compared to etching in 10 mL. For Mg-5Gd (Figure 9b), the machining marks are still visible after the 10 mL etching in contrast to 5 mL etching and the number of pits/mm^2 (Table 4) is lower accompanied by smaller standard deviation. Almost no machining marks are visible for the Mg-10Gd (Figure 9c). Here, using 5 mL solution led to more pits/mm^2 (Table 4) than using 10 mL solution. Table 4 shows that for 5 mL volume of etching solution the number of pits clearly decreases with increasing Gd content, while for 10 mL solution the number of pits is comparable within the standard deviation. It should be noted, that the color code refers to different absolute heights depending on the image.

Table 4. Number of etching pits formed in the Mg-*x*Gd alloys after etching for 150 s in 5 and 10 mL solutions.

Condition	Mg-2Gd	Mg-5Gd	Mg-10Gd
pits/mm^2 for 5 mL	2.66 ± 0.51	1.70 ± 1.11	0.99 ± 0.41
pits/mm^2 for 10 mL	0.21 ± 0.30	0.20 ± 0.00	0.52 ± 0.46

3.6. ToF-SIMS

Dynamic SIMS measurements were used to analyze the depth distribution of Fe impurities in the topmost 0.3 µm of the untreated, as received samples. For this, on each of two samples for Mg-2Gd, Mg-5Gd and Mg-10Gd, three depth profiles were analyzed. As example for a depth profile, only one profile of each alloy (Mg-2Gd, Mg-5Gd, Mg-10Gd_a) is shown in Figure 10. The depth profiles of the as-received Mg-*x*Gd samples, indicate a higher intensity of Fe measured in near surface region as compared to the bulk of the alloys. After a maximum Fe signal at around 30 nm of erosion, a decrease in Fe^+ counts was observed. The initial increase of the Fe signals is based on airborne contaminations, shielding effectively signals from deeper layers due to the low probing depth of SIMS. As soon as this contamination layer is removed, and the sputter/implantation equilibrium of oxygen reached, the Fe signals are dropping as shown in Figure 10. A second profile of Mg-10Gd_b (Figure 10) is plotted as further example, where next to Fe as surface contamination, also Fe particles inside the bulk are detected (Figure 11 d–f). For this reason, the decrease in Fe intensity is not as strong as shown for Mg-10Gd_a after 340 nm.

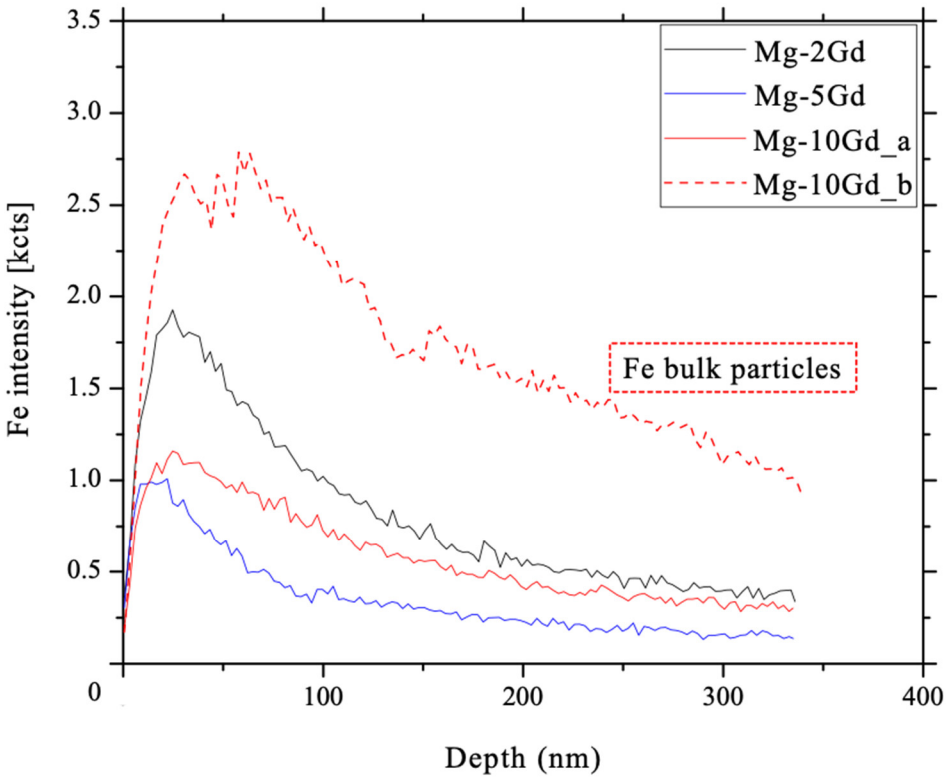

Figure 10. Depth profiles for Fe in the sub-surface of as-received Mg-*x*Gd alloys. The Fe intensity decreases at a depth around 30 nm. One profile of each alloy (Mg-2Gd, Mg-5Gd, Mg-10Gd_a) is plotted and show the decrease of Fe intensity to be virtually zero for the case of Fe surface contamination. The decrease of Mg-10Gd_b is not virtually zero after around 340 nm, due to additional bigger Fe particles inside the bulk.

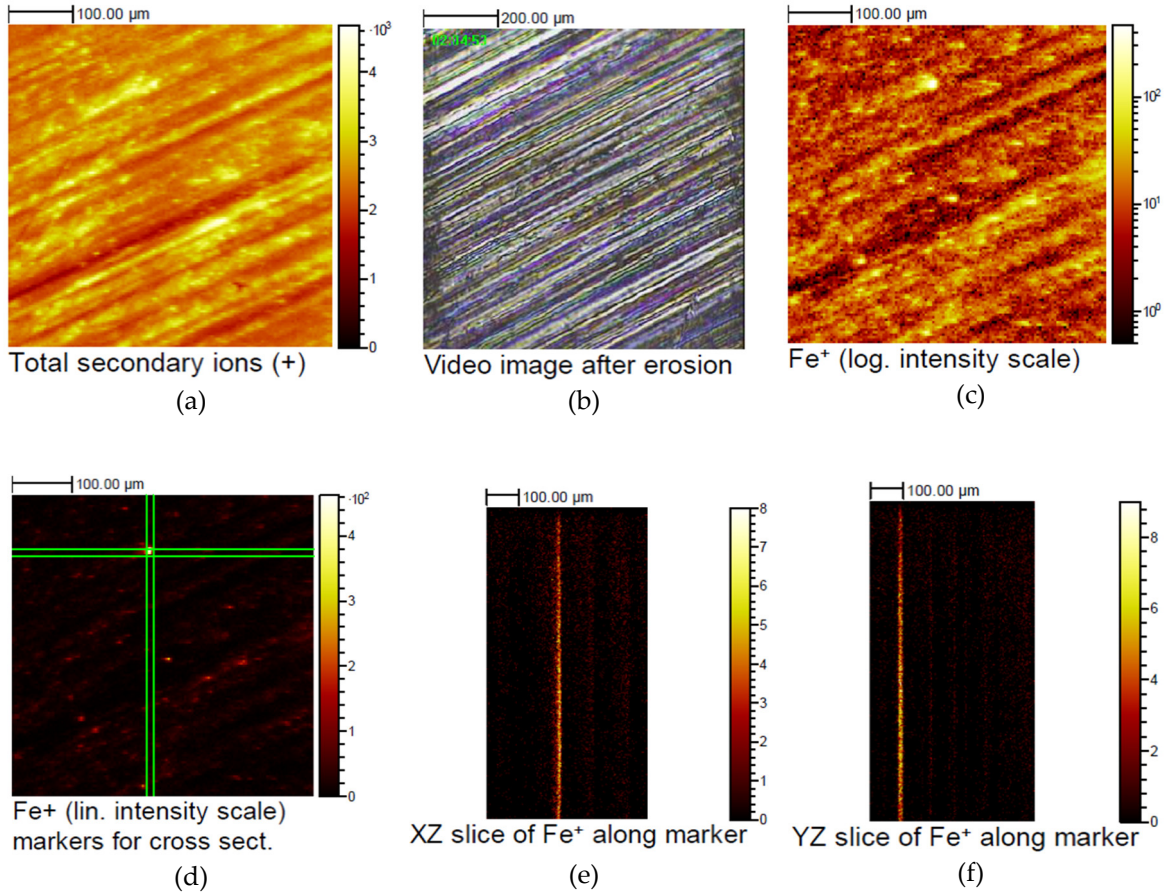

Figure 11. Lateral distribution of the Fe containing inclusions in Mg-10Gd corresponding to the depth profile: (**a**) total secondary ion image; (**b**) micrograph showing the measurement position; (**c**) depth-integrated lateral distribution of Fe with a log intensity scale; (**d**) integrated Fe signal with linear intensity scale, highlighting an individual Fe particle; (**e**) calculated cross sections in the XZ plane along the green indicators centered on the Fe particle; (**f**) calculated cross sections in the YZ plane along the green indicators centered on the Fe particle.

Analyzing the lateral distribution of the Fe containing inclusions two contributions are detectable: (a) is a weak Fe background correlated with the surface structure from the sample preparation, and (b) some rare individual Fe particles of several µm size. Figure 11 shows data corresponding to the depth profile shown in Figure 10. Mg-10Gd_b with the highest Fe intensity in Figure 10 shows the total secondary ion image (Figure 11a), a video image showing the measurement position (Figure 11b), and in Figure 11c the depth-integrated lateral distribution of Fe is given with a log intensity scale. In Figure 11d, the depth-integrated Fe signal is shown again, here with linear intensity scale, highlighting an individual Fe particle bracketed by green lines. Both panels in Figure 11e and f are calculated cross sections in the XZ and YZ plane along the green indicators centered on the Fe particle. As seen from the cross sections, the Fe particle is not eroded by the ion bombardment and is responsible for the remarkably strong Fe signal (Mg-10Gd_b) decreasing only very slowly during depth profiling in Figure 10.

After etching with HAc, much more material is removed than during the dynamic SIMS experiments reaching only 0.34 µm depth. At the etched surface (15 s and 150 s) of the alloys Fe almost completely disappeared in case of the Mg-2Gd and Mg-5Gd alloys (Figure 12). Here, the intensity of Fe on the surface after etching was found to be rather uniform as indicated by analysis of several positions. In contrast, a slightly greater local variation of the Fe signal was observed in the etched Mg-10Gd alloy. However, after etching the Gd rich samples the scatter of the Fe detected atdifferent

measurement positions decreased in comparison to the AR samples. The remaining Fe content after etching of Mg-10Gd was reduced but still higher as compared to the samples with lower Gd content.

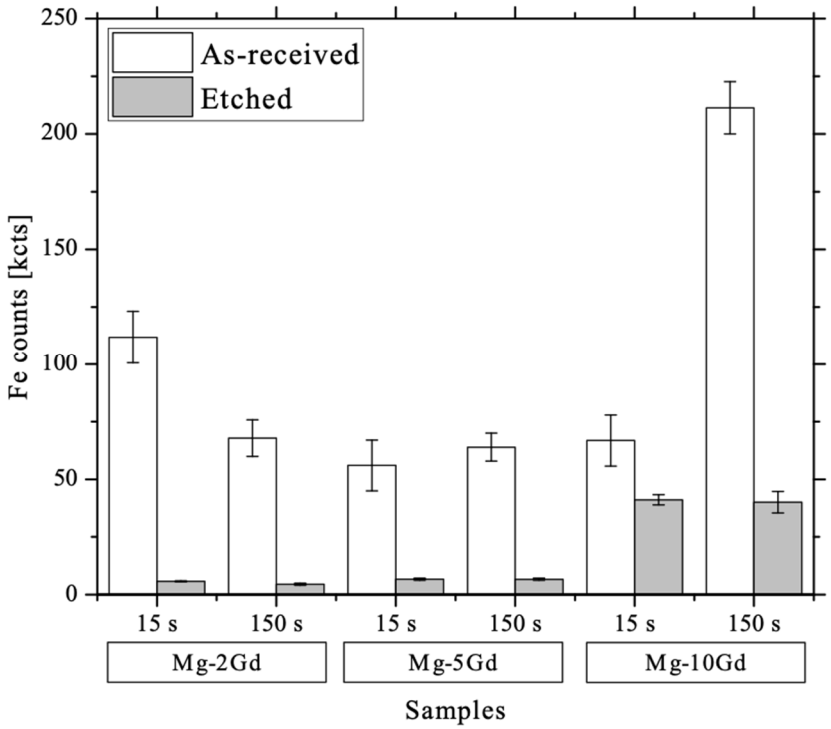

Figure 12. Graph showing Fe counts at the surface before and after etching the different alloys, obtained using ToF-SIMS.

4. Discussion

The sum of DZ and TZ depths (Figure 4a) is decreasing with increasing Gd amount, due to the higher strength of the material [47]. Higher Gd amounts strengthen the material by solid solution strengthening [51]. Higher strength lead to lower deformation depths, which results in reaching the bulk material earlier by etching for Mg-10Gd than for the other alloys. A higher dependency of TZ than of DZ on Gd content is expected, due to the not significant difference of DZ between different Gd amounts. Kaynak et al. [37] also reported a segmentation into three different microstructures after machining, whose thicknesses correlate with the mechanical properties of the alloy and the cutting conditions and parameters. Severe plastic deformation is described for refined and transition layer in near surface region, followed by the bulk material. Lu et al. [52] described a stress layer depth in near surface region of AZ31, visible by varying microstructure in contrast to the bulk material. The stress layer depth increased with decreased cutting speed. In the present study, all alloys are separated into two zones. The DZ is a strong deformation in direct surface region, where grains are not visible by SEM. It is assumed, that the original grain structure is damaged by the cutting tool. For the reason, that DZ is similar for all Gd content, it is supposed that the strength of the alloys has a lower effect on DZ. The cutting parameters are equal, which means the same force is introduced into the material and grains are crushed and shifted similarly, despite higher tensile strength of the alloys. With higher strength, dislocations are slipping less, which is why, TZ is more affected on depth than DZ. The second zone TZ in the sub-surface is the accumulation of twins, where twinning is a process to enable more material plasticity [53]. After twinning, the bulk material with non-deformed grains follows, similar to Kaynak et al. [37]. Residual stress is expected in the direct and sub-surface, which is not further investigated in this study.

More surface material is removed during the etching process with a higher Gd content (Figure 4b). The thicker TZ for alloys with lower Gd content (Figure 4a) might slow down dissolution at early

stages. For Mg-10Gd, the twinned surface region is removed earlier as compared to alloys with lower Gd contents. Hence the un-twinned bulk material is reached faster, due to a smaller TZ thickness. Some studies [54–56] reported the corrosion resistance to be increased by reduced grain size, and due to grain boundaries acting as borders between grains [54]. Corrosion in neutral and acid solutions are both electrochemical processes, for what the principle of mentioned corrosion studies are assumed to be transferable on HAc etching. Under the assumption that a higher twinning density results in higher number of twin boundaries, which act similar to grain boundaries, it would be expected that the material dissolution rate would be reduced in twinned material compared to un-twinned bulk.

By etching for 15 s only, less material is removed (Figure 4b) and no pit formation occurs (Figure 8b). Pit forming is observed for etching with 150 s duration (Figure 9, Table 4), associated with higher material removal. A chemical or structural difference inside an Mg alloy can result in a potential difference, where different parts of the material show either anodic or cathodic behavior. Grains and grain boundaries, as well as deformed and non-deformed areas, different crystallographic orientation or secondary phases can thus all lead to inhomogeneous dissolution [57–61]. It is assumed that Gd particles act as cathodes as well, due to Gd rich accumulations inside the etching pits (Figure 5). The visible accumulation of Gd after etching is possibly justified by the non-dissolution of Gd rich particles in HAc. The more material is removed by etching the more particles are freed from the matrix and can serve as potential initiators for pit forming. Pit forming in 5 mL solution etching is intensified in contrast to 10 mL solution. It is reported, that pit forming is released at a specific temperature for metals [62] and in general the corrosion rate increased with increasing temperature [63]. Hence, the temperature plays a pivotal role during pit formation in acid solution, the material removal is not the only limiting factor for pit forming.

It is reported, that the amount of Gd rich particles like GdH_2 is increasing with Gd addition inside the alloy [20]. For that reason, a higher number of pits would be expected, by considering Gd rich particles as the only initiation. Owing to a contrary pit forming behavior (Figure 9 and Table 4), it is assumed, that a temperature increase during etching for Mg-2Gd and Mg-5Gd has a higher influence on pit forming than hydrides. For this reason, it is expected that by regulating the etching temperature, pit forming will be reduced or avoided. The etching procedure may be then transferred to other RE systems.

The acceleration of the reaction, despite the neutralization of acetic acid leading to an increase of the pH of the solution (Table 3) is explained by the strong temperature increase measured directly at the metal surface in solution (in that case from 16 °C at the beginning to 56 °C after 150 s etching, Figure 7). The exothermic nature of the etching reactions leads to a temperature increase during the process. Neglecting the heat loss to the surrounding, the temperature difference observed during the etching process is dependent on the etch rate and the heat capacity of the setup, mainly the etchant solution. During etching with 5 mL of solution, the temperature increase is higher and more pits are formed compared to etching 15 s or 150 s in 10 mL etching (Figure 7).

Removal of the DZ and TZ is assumed to generate more heat compared to the removal of un-twinned bulk material. The Mg-2Gd alloy with highest temperature increase (Figure 7) had the highest twinning depth which was not completely removed even after the longest etching time in 5 mL solution (Figure 4a,b). Comparable material removal between samples etched in 5 mL and 10 mL of solution after the same time, suggest similar dissolution rates of the material. Etching in 10 mL solution did not show the same strong increase, due to higher thermal capacity of 10 mL solution compared to 5 mL.

After pits form, the roughness increases compared to the AR condition and 15 s etched samples (Figures 8 and 9). In particular, the Mg-2Gd alloy with the highest number of pits, exhibited the highest surface roughness Sa (Figure 9a). Higher roughness is attributed to pit formation, resulting in higher difference between peaks and valleys. The roughness of a surface may have influence of the initial degradation of an implant or improve cell density or is even useful to vary the morphology of

coatings [64–67]. For this reason, a variation of etching parameter allows the formation of a required morphology, dependent on the application.

Nwaogu et al. [31] reported that a rougher surface after etching arises from the dissolution of grain boundaries. Hou et al. [68] determined a higher attack of hydrofluoric acid (HF) for microstructure that contained more twins compared to less twinned specimens. The roughness of a sample with a high twinning density increased after dipping in HF for longer times. More heavily twinned samples gave rise to a higher surface roughness [68]. Because of that, twinning is assumed to influence pit forming, associated in higher surface roughness. Wang et al. [59] suggest that galvanic corrosion can take place between twinned and un-twinned microstructural regions due to different crystallographic orientations. Aung and Zhou [54] reported higher inter-granular corrosion in twinned regions, but more pits forming within un-twinned microstructure. The density of twins is higher within the material at the near surface region. Pit forming is expected for regions with less dense twinning, where galvanic corrosion can occur between twinned and un-twinned regions. As shown in Figure 3c, after etching of Mg-10Gd, only the bulk material is visible, while for Mg-2Gd there are areas of twinning, bulk material and a more uneven etched surface after 150 s etching (Figure 3a). The standard deviation of TZ is increasing with decreasing Gd amount (Figure 4a), because of strong varying twin depth on different positions in Mg-2Gd. The TZ of Mg-10Gd is more accumulated and flatter (Figure 2a). By removing less material for Mg-2Gd, deeper twins are still visible, next to areas, where flat TZ are already removed (Figure 3a). With a higher number of pits in Mg-2Gd it is expected, that the suggestions of Wang et al. [59] coincidences with the results in this study. It is expected that pits can occur due to the dissolution of the matrix between grain boundaries inside DZ and TZ area. It is assumed, that non-deformed grains dissolve locally faster compared to twinned grains as supposed before with different material dissolutions rates of DZ, TZ and bulk material.

The milling process introduces Fe impurities on the outer surface. This is shown by the ToF-SIMs experiments which indicate higher Fe ion counts near the surface region compared to those obtained inside the bulk material (Figure 10). Fe impurities must be removed from the surface to avoid galvanic corrosion, resulting in non-homogenous corrosion and fast material removal especially in the initial state [34]. By reducing the initial corrosion rate, mechanical integrity and ongrowth of the implant is ensured. Gawlik et al. [45] reported that HAc etching reduce the scattering of degradation results compared to untreated samples. This can be explained by the results of the reduction of Fe contamination in the present study. Using HAc etching for 15 s on the Mg-*x*Gd alloys resulted in the surfaces being free of Fe contaminants (Figure 12) once a layer of around 2–9 µm thickness was removed from the surface. Supplit el al. [46] support the use of acid treatments as a surface cleaning method [46]. Nwaogu et al. [31] showed that removing 4 µm material was enough to reduce the number of contaminants present, including Fe and Ni, and resulted in lower corrosion rates. It can be assumed that acetic acid etching is able to remove contaminants such as Fe from the material surfaces, by removing the near surface region due to the solubility of Fe in acid [69–71]. The etching time had no influence on the amount of Fe on the surfaces, the number of Fe counts was similarly reduced after 15 s and 150 s (Figure 12). As a result, it is not necessary to remove more than 9 µm from the surface, achieved by longer etching times. The lateral distribution of Fe in the near surface region after etching is assumed to be homogenous for the Mg-2Gd and Mg-5Gd alloys, as there was a lower standard deviation in the number of counts measured at different positions on the specimen. Etching the Mg-10Gd greatly reduced the intensity of Fe counts obtained for different samples, even if the intensity varyied strongly in the as-received condition. These results indicate that the etching process is advantageous in removing surface Fe. Due to higher number of Fe counts obtained in the Mg-10Gd compared to the other alloys, it is assumed, that Fe particles are more numerous at the surface and distributed to deeper regions within the alloy. This assumption is confirmed by AAS measurements of Harmuth et al. [47], which shows higher Fe bulk content of Mg-10Gd compared to Mg-2Gd and Mg-5Gd.

5. Conclusions

Acetic acid etching works of Mg-Gd alloys for biological and engineer applications and is expected to be used as surface treatment for other RE–alloys as well. The following should be considered:

- Short etching durations like 15 s induce no pit formation and are suitable for smooth surfaces like rolled sheets.
- Rougher surfaces are generated by use of longer etching time of 150 s or an etching volume of 5 mL instead of 10 mL and can encourage cell adhesion.
- HAc is capable to reliably remove surface contaminations like Fe after 15 s and 150 s, which is why a minor material removal of 2–9 µm is sufficient. According to previous reported research, material removal can reduce the scatter of degradation results.
- The removal of deformed material from processing is enabled by use of higher etching time. The deformation depth depends on the amount of Gd.
- Different etching kinetics are expected from deformed to non-deformed microstructure, which are regulated by the heat dissipation into the environment.
- The number of Gd rich particles is not the leading reason for pitting, but Gd particles and twins act as an initiator for pit forming, caused by an increase in temperature. The temperature of the exothermic reaction has the highest impact on pit formation.

Author Contributions: M.M.G. and B.W. conceived and designed the experiments; M.M.G., V.D., J.G., J.H. and A.W. performed the experiments; M.M.G., B.W., V.D. and A.W. analyzed the data; B.W., A.W. and J.H. contributed reagents/materials/analysis tools; M.M.G. wrote the initial manuscript; B.W., J.G., V.D., T.E., A.W., and R.W.-R. revised the manuscript; M.M.G. prepared the final paper.

Funding: This research was financially supported by the Helmholtz Virtual Institute VH-VI-523 (In vivo studies of biodegradable Mg based implant materials).

Acknowledgments: The authors would like to thank the department of Corrosion and Surface Technology, Helmholtz-Zentrum Geesthacht, Germany and Karlsruhe Nano Micro Facility (KNMF), Germany.

Conflicts of Interest: The authors declare no conflict of interest. The funders had no role in the design of the study; in the collection, analyses, or interpretation of data; in the writing of the manuscript, and in the decision to publish the results.

References

1. Mao, L.; Shen, L.; Chen, J.; Zhang, X.; Kwak, M.; Wu, Y.; Fan, R.; Zhang, L.; Pei, J.; Yuan, G.; et al. A promising biodegradable magnesium alloy suitable for clinical vascular stent application. *Sci. Rep.* **2017**, *7*, 46343. [CrossRef] [PubMed]
2. Persaud-Sharma, D.; McGoron, A. Biodegradable Magnesium Alloys: A Review of Material Development and Applications. *J. Biomim. Biomater. Tissue Eng.* **2012**, *12*, 25–39. [CrossRef] [PubMed]
3. Witte, F.; Hort, N.; Vogt, C.; Cohen, S.; Kainer, K.U.; Willumeit, R.; Feyerabend, F. Degradable biomaterials based on magnesium corrosion. *Curr. Opin. Solid State Mater. Sci.* **2008**, *12*, 63–72. [CrossRef]
4. Witte, F.; Kaese, V.; Haferkamp, H.; Switzer, E.; Meyer-Lindenberg, A.; Wirth, C.J.; Windhagen, H. In vivo corrosion of four magnesium alloys and the associated bone response. *Biomaterials* **2005**, *26*, 3557–3563. [CrossRef] [PubMed]
5. Galli, S.; Stocchero, M.; Andersson, M.; Karlsson, J.; He, W.; Lilin, T.; Wennerberg, A.; Jimbo, R. The effect of magnesium on early osseointegration in osteoporotic bone: A histological and gene expression investigation. *Osteoporos. Int.* **2017**, *28*, 2195–2205. [CrossRef] [PubMed]
6. Castellani, C.; Lindtner, R.A.; Hausbrandt, P.; Tschegg, E.; Stanzl-Tschegg, S.E.; Zanoni, G.; Beck, S.; Weinberg, A.-M. Bone–implant interface strength and osseointegration: Biodegradable magnesium alloy versus standard titanium control. *Acta Biomater.* **2011**, *7*, 432–440. [CrossRef] [PubMed]
7. Liu, C.; Ren, Z.; Xu, Y.; Pang, S.; Zhao, X.; Zhao, Y. Biodegradable Magnesium Alloys Developed as Bone Repair Materials: A Review. *Scanning* **2018**, *2018*, 15. [CrossRef] [PubMed]
8. Feyerabend, F.; Wendel, H.-P.; Mihailova, B.; Heidrich, S.; Agha, N.A.; Bismayer, U.; Willumeit-Römer, R. Blood compatibility of magnesium and its alloys. *Acta Biomater.* **2015**, *25*, 384–394. [CrossRef]

9. Feyerabend, F.; Fischer, J.; Holtz, J.; Witte, F.; Willumeit, R.; Drücker, H.; Vogt, C.; Hort, N. Evaluation of short-term effects of rare earth and other elements used in magnesium alloys on primary cells and cell lines. *Acta Biomater.* **2010**, *6*, 1834–1842. [CrossRef]
10. Li, J.; Tan, L.; Wan, P.; Yu, X.; Yang, K. Study on microstructure and properties of extruded Mg–2Nd–0.2Zn alloy as potential biodegradable implant material. *Mater. Sci. Eng. C* **2015**, *49*, 422–429. [CrossRef]
11. Hort, N.; Huang, Y.; Fechner, D.; Störmer, M.; Blawert, C.; Witte, F.; Vogt, C.; Drücker, H.; Willumeit, R.; Kainer, K.U. Magnesium alloys as implant materials—Principles of property design for Mg–RE alloys. *Acta Biomater.* **2010**, *6*, 1714–1725. [CrossRef] [PubMed]
12. Rokhlin, L.L. *Magnesium Alloys Containing Rare Earth Metals: Structure and Properties*; Advances in Metallic Alloys; Taylor & Francis: London, UK; New York, NY, USA, 2003; ISBN 978-0-415-28414-1.
13. Hamdy Makhlouf, A.S.; Hussien, H.M. Deposition, Characterization and Electrochemical Properties of Permanganate-Based Coating Treatments Over ZE41 Mg-Zn-Rare Earth Alloy. *Int. J. Electrochem. Sci.* **2013**, *8*, 11386–11402.
14. Hamdy Makhlouf, A.S.; Hussien, H.M. The effect of solution pH of permanganate coating on the electrochemical characteristics of ZE41 magnesium alloy in chloride media. *Int. J. Electrochem. Sci.* **2014**, *9*, 2682–2695.
15. Hamdy Makhlouf, A.S. Intelligent Stannate-Based Coatings of Self-Healing Functionality for Magnesium Alloys. In *Intelligent Coatings for Corrosion Control*; Tiwari, A., Rawlins, J., Hihara, L.H., Eds.; Butterworth-Heinemann: Boston, MA, USA, 2015; pp. 537–555. ISBN 978-0-12-411467-8.
16. Hamdy, A.S.; Doench, I.; Möhwald, H. Vanadia-based coatings of self-repairing functionality for advanced magnesium Elektron ZE41 Mg–Zn–rare earth alloy. *Surf. Coat. Technol.* **2012**, *206*, 3686–3692. [CrossRef]
17. Hamdy, A.S.; Doench, I.; Möhwald, H. Assessment of a one-step intelligent self-healing vanadia protective coatings for magnesium alloys in corrosive media. *Electrochim. Acta* **2011**, *56*, 2493–2502. [CrossRef]
18. Hamdy, A.S.; Butt, D.P. Corrosion mitigation of rare-earth metals containing magnesium EV31A-T6 alloy via chrome-free conversion coating treatment. *Electrochim. Acta* **2013**, *108*, 852–859. [CrossRef]
19. Peng, Q.; Huang, Y.; Meng, J.; Li, Y.; Kainer, K.U. Strain induced GdH2 precipitate in Mg–Gd based alloys. *Intermetallics* **2011**, *19*, 382–389. [CrossRef]
20. Huang, Y.; Yang, L.; You, S.; Gan, W.; Kainer, K.U.; Hort, N. Unexpected formation of hydrides in heavy rare earth containing magnesium alloys. *J. Magnes. Alloy.* **2016**, *4*, 173–180. [CrossRef]
21. Zhu, S.M.; Nie, J.F.; Gibson, M.A.; Easton, M.A. On the unexpected formation of rare earth hydrides in magnesium–rare earth casting alloys. *Scr. Mater.* **2014**, *77*, 21–24. [CrossRef]
22. Yang, L.; Feyerabend, F.; Kainer, K.U.; Willumeit, R.; Hort, N. Corrosion Behavior of As-Cast Binary Mg-Dy Alloys. *Mater. Sci. Forum* **2011**, *690*, 417–421. [CrossRef]
23. Yang, L.; Huang, Y.; Peng, Q.; Feyerabend, F.; Kainer, K.U.; Willumeit, R.; Hort, N. Mechanical and corrosion properties of binary Mg–Dy alloys for medical applications. *Mater. Sci. Eng. B* **2011**, *176*, 1827–1834. [CrossRef]
24. Yang, L.; Huang, Y.; Feyerabend, F.; Willumeit, R.; Kainer, K.U.; Hort, N. Influence of ageing treatment on microstructure, mechanical and bio-corrosion properties of Mg–Dy alloys. *J. Mech. Behav. Biomed. Mater.* **2012**, *13*, 36–44. [CrossRef] [PubMed]
25. Yang, L.; Hort, N.; Laipple, D.; Höche, D.; Huang, Y.; Kainer, K.U.; Willumeit, R.; Feyerabend, F. Element distribution in the corrosion layer and cytotoxicity of alloy Mg–10Dy during in vitro biodegradation. *Acta Biomater.* **2013**, *9*, 8475–8487. [CrossRef] [PubMed]
26. Yang, L.; Huang, Y.; Feyerabend, F.; Willumeit, R.; Mendis, C.; Kainer, K.U.; Hort, N. Microstructure, mechanical and corrosion properties of Mg–Dy–Gd–Zr alloys for medical applications. *Acta Biomater.* **2013**, *9*, 8499–8508. [CrossRef] [PubMed]
27. Willumeit-Römer, R.; Moosmann, J.; Zeller-Plumhoff, B.; Florian Wieland, D.C.; Krüger, D.; Wiese, B.; Wennerberg, A.; Peruzzi, N.; Galli, S.; Beckmann, F.; et al. Visualization of Implant Failure by Synchrotron Tomography. In *TMS 2018 147th Annual Meeting & Exhibition Supplemental Proceedings*; The Minerals, Metals & Materials Society, Ed.; Springer: Cham, Switzerland, 2018; pp. 275–284. ISBN 978-3-319-72525-3.
28. Moosmann, J.; Zeller-Plumhoff, B.; Florian Wieland, D.C.; Galli, S.; Krüger, D.; Dose, T.; Burmester, H.; Wilde, F.; Bech, M.; Peruzzi, N.; et al. Biodegradable magnesium-based implants in bone studied by synchrotron radiation microtomography. In *Proceedings of the Developments in X-Ray Tomography XI*; Müller, B., Wang, G., Eds.; SPIE: San Diego, CA, USA, 2017.

29. Galli, S.; Hammel, J.U.; Herzen, J.; Damm, T.; Jimbo, R.; Beckmann, F.; Wennerberg, A.; Willumeit-Römer, R. Evaluation of the degradation behavior of resorbable metal implants for in vivo osteosynthesis by synchrotron radiation based X-ray tomography and histology. In *Developments in X-Ray Tomography X*; Stock, S.R., Müller, B., Wang, G., Eds.; SPIE: San Diego, CA, USA, 2016.
30. Song, G.-L.; Xu, Z. The surface, microstructure and corrosion of magnesium alloy AZ31 sheet. *Electrochim. Acta* **2010**, *55*, 4148–4161. [CrossRef]
31. Nwaogu, U.C.; Blawert, C.; Scharnagl, N.; Dietzel, W.; Kainer, K.U. Effects of organic acid pickling on the corrosion resistance of magnesium alloy AZ31 sheet. *Corros. Sci.* **2010**, *52*, 2143–2154. [CrossRef]
32. Nwaogu, U.C.; Blawert, C.; Scharnagl, N.; Dietzel, W.; Kainer, K.U. Influence of inorganic acid pickling on the corrosion resistance of magnesium alloy AZ31 sheet. *Corros. Sci.* **2009**, *51*, 2544–2556. [CrossRef]
33. Gray-Munro, J.E.; Seguin, C.; Strong, M. Influence of surface modification on the in vitro corrosion rate of magnesium alloy AZ31. *J. Biomed. Mater. Res. Part A* **2009**, *91A*, 221–230. [CrossRef]
34. Höche, D.; Blawert, C.; Lamaka, S.V.; Scharnagl, N.; Mendis, C.; Zheludkevich, M.L. The effect of iron re-deposition on the corrosion of impurity-containing magnesium. *Phys. Chem. Chem. Phys.* **2016**, *18*, 1279–1291. [CrossRef]
35. Denkena, B.; Lucas, A. Biocompatible Magnesium Alloys as Absorbable Implant Materials—Adjusted Surface and Subsurface Properties by Machining Processes. *CIRP Ann. Manuf. Technol.* **2007**, *56*, 113–116. [CrossRef]
36. Denkena, B.; Lucas, A.; Thorey, F.; Waizy, H.; Angrisani, N.; Meyer-Lindenberg, A. Biocompatible Magnesium Alloys as Degradable Implant Materials—Machining Induced Surface and Subsurface Properties and Implant Performance. In *Special Issues on Magnesium Alloys*; Monteiro, W.A., Ed.; InTech: London, UK, 2011; ISBN 978-953-307-391-0.
37. Kaynak, Y.; Lu, T.; Jawahir, I.S. Cryogenic Machining-Induced Surface Integrity: A Review and Comparison with Dry, MQL, and Flood-Cooled Machining. *Mach. Sci. Technol.* **2014**, *18*, 149–198. [CrossRef]
38. Liu, Y.; Liu, D.; You, C.; Chen, M. Effects of grain size on the corrosion resistance of pure magnesium by cooling rate-controlled solidification. *Front. Mater. Sci.* **2015**, *9*, 247–253. [CrossRef]
39. Ahmadkhaniha, D.; Fedel, M.; Heydarzadeh Sohi, M.; Deflorian, F. Corrosion behavior of severely plastic deformed magnesium based alloys: A review. *Surf. Eng. Appl. Electrochem.* **2017**, *53*, 439–448. [CrossRef]
40. Pu, Z.; Outeiro, J.C.; Batista, A.C.; Dillon, O.W.; Puleo, D.A.; Jawahir, I.S. Enhanced surface integrity of AZ31B Mg alloy by cryogenic machining towards improved functional performance of machined components. *Int. J. Mach. Tools Manuf.* **2012**, *56*, 17–27. [CrossRef]
41. Marchkesbery, W.R.; Ehmann, W.D.; Hossain, T.I.M.; Alauddin, M.; Goodin, D.T. Instrumental neutron activation analysis of brain aluminum in Alzheimer's disease and aging. *Ann. Neurol.* **1981**, *10*, 511–516. [CrossRef] [PubMed]
42. Crapper, D.R.; Krishnan, S.S.; Quittkat, S. Aluminium, neurofibrillary degeneration and alzheimer's disease. *Brain* **1976**, *99*, 67–80. [CrossRef]
43. Mirza, A.; King, A.; Troakes, C.; Exley, C. Aluminium in brain tissue in familial Alzheimer's's disease. *J. Trace Elem. Med. Biol.* **2017**, *40*, 30–36. [CrossRef]
44. Tomljenovic, L. Aluminum and Alzheimer's Disease: After a Century of Controversy, Is there a Plausible Link? *J. Alzheimers Dis.* **2011**, *23*, 567–598. [CrossRef]
45. Gawlik, M.M.; Steiner, M.; Wiese, B.; González, J.; Feyerabend, F.; Dahms, M.; Ebel, T.; Willumeit-Römer, R. The effects of HAc etching on the degradation behavior of Mg-5Gd. *J. Med. Mater. Technol.* **2017**, *1*, 22–25.
46. Supplit, R.; Koch, T.; Schubert, U. Evaluation of the anti-corrosive effect of acid pickling and sol–gel coating on magnesium AZ31 alloy. *Corros. Sci.* **2007**, *49*, 3015–3023. [CrossRef]
47. Harmuth, J.; Wiese, B.; Bohlen, J.; Ebel, T.; Willumeit-Römer, R. Tailoring of Material Properties of Mg-Gd Alloys for Biomedical Applications. In *Magnesium 2018: Proceedings of the 11th International Conference on Magnesium Alloys and Their Applications*; Brunel University: London, UK, 2018; ISBN 978-1-908549-37-2.
48. *Characterisation of Areal Surface Texture*; Leach, R. (Ed.) Springer: Berlin/Heidelberg, Germany, 2013; ISBN 978-3-642-36457-0.
49. Yamamura, Y.; Tawara, H. Energy dependence of ion-induced sputtering yields from monatomic solids at normal incidence. *At. Data Nucl. Data Tables* **1996**, *62*, 149–253. [CrossRef]
50. Kubásek, J.; Vojtěch, D. Structural and corrosion characterization of biodegradable Mg–RE (RE = Gd, Y, Nd) alloys. *Trans. Nonferrous Met. Soc. China* **2013**, *23*, 1215–1225. [CrossRef]

51. Askeland, D.R. *Essentials of Materials Science and Engineering*; Third Edition, SI.; Cengage Learning: Stamford, CT, USA, 2014; ISBN 978-1-111-57686-8.
52. Lu, L.; Hu, S.; Liu, L.; Yin, Z. High speed cutting of AZ31 magnesium alloy. *J. Magnes. Alloy.* **2016**, *4*, 128–134. [CrossRef]
53. Barnett, M.R. Twinning and the ductility of magnesium alloys. *Mater. Sci. Eng. A* **2007**, *464*, 1–7. [CrossRef]
54. Aung, N.N.; Zhou, W. Effect of grain size and twins on corrosion behaviour of AZ31B magnesium alloy. *Corros. Sci.* **2010**, *52*, 589–594. [CrossRef]
55. Alvarez-Lopez, M.; Pereda, M.D.; del Valle, J.A.; Fernandez-Lorenzo, M.; Garcia-Alonso, M.C.; Ruano, O.A.; Escudero, M.L. Corrosion behaviour of AZ31 magnesium alloy with different grain sizes in simulated biological fluids. *Acta Biomater.* **2010**, *6*, 1763–1771. [CrossRef] [PubMed]
56. Birbilis, N.; Ralston, K.D.; Virtanen, S.; Fraser, H.L.; Davies, C.H.J. Grain character influences on corrosion of ECAPed pure magnesium. *Corros. Eng. Sci. Technol.* **2010**, *45*, 224–230. [CrossRef]
57. Bergmann, W.; Leyens, C.; Fleck, C. *Werkstofftechnik: Grundlagen und Anwendung. Teil 1: Grundlagen*; Hanser: München, Germany, 2013; ISBN 978-3-446-43581-0.
58. Merkel, M.; Thomas, K.-H. *Taschenbuch der Werkstoffe*; 7 Verbesserte Auflage; Fachbuchverlag Leipzig im Carl Hanser Verlag: München, Germany, 2008; ISBN 978-3-446-41194-4.
59. Wang, B.J.; Xu, D.K.; Dong, J.H.; Ke, W. Effect of the crystallographic orientation and twinning on the corrosion resistance of an as-extruded Mg–3Al–1Zn (wt.%) bar. *Scr. Mater.* **2014**, *88*, 5–8. [CrossRef]
60. Zou, G.; Peng, Q.; Wang, Y.; Liu, B. The effect of extension twinning on the electrochemical corrosion properties of Mg–Y alloys. *J. Alloy. Compd.* **2015**, *618*, 44–48. [CrossRef]
61. Pawar, S.; Slater, T.J.A.; Burnett, T.L.; Zhou, X.; Scamans, G.M.; Fan, Z.; Thompson, G.E.; Withers, P.J. Crystallographic effects on the corrosion of twin roll cast AZ31 Mg alloy sheet. *Acta Mater.* **2017**, *133*, 90–99. [CrossRef]
62. Frankel, G.S. Pitting Corrosion of Metals. *J. Electrochem. Soc.* **1998**, *145*, 2186. [CrossRef]
63. *Corrosion: Fundamentals, Testing and Prevention*; ASM Handbook; ASM International; Cramer, S.D.; Covino, B.S., Jr. (Eds.) ASM International: Materials Park, OH, USA, 2003; ISBN 978-0-87170-705-5.
64. Gawlik, M.; Wiese, B.; Desharnais, V.; Ebel, T.; Willumeit-Römer, R. The Effect of Surface Treatments on the Degradation of Biomedical Mg Alloys—A Review Paper. *Materials* **2018**, *11*, 2561. [CrossRef] [PubMed]
65. Lorenz, C.; Brunner, J.G.; Kollmannsberger, P.; Jaafar, L.; Fabry, B.; Virtanen, S. Effect of surface pre-treatments on biocompatibility of magnesium. *Acta Biomater.* **2009**, *5*, 2783–2789. [CrossRef] [PubMed]
66. Yoo, B.; Shin, K.R.; Hwang, D.Y.; Lee, D.H.; Shin, D.H. Effect of surface roughness on leakage current and corrosion resistance of oxide layer on AZ91 Mg alloy prepared by plasma electrolytic oxidation. *Appl. Surf. Sci.* **2010**, *256*, 6667–6672. [CrossRef]
67. Walter, R.; Kannan, M.B.; He, Y.; Sandham, A. Effect of surface roughness on the in vitro degradation behaviour of a biodegradable magnesium-based alloy. *Appl. Surf. Sci.* **2013**, *279*, 343–348. [CrossRef]
68. Hou, Y.; Li, Y.; Zhang, C.; Koizumi, Y.; Chiba, A. Effects of cold working on corrosion resistance of Co-modified Ni–16Cr–15Mo alloy in hydrofluoric acid solution. *Corros. Sci.* **2014**, *89*, 258–267. [CrossRef]
69. McCafferty, E. *Introduction to Corrosion Science*; Springer: New York, NY, USA, 2010; ISBN 978-1-4419-0454-6.
70. Chen, H.; Grassian, V.H. Iron Dissolution of Dust Source Materials during Simulated Acidic Processing: The Effect of Sulfuric, Acetic, and Oxalic Acids. *Environ. Sci. Technol.* **2013**, *47*, 10312–10321. [CrossRef] [PubMed]
71. *Allgemeines zur Pharmakologie der Metalle—Eisen—Mangan—Kobalt—Nickel*; Heffter, A. (Ed.) Springer: Berlin/Heidelberg, Germany, 1934; ISBN 978-3-642-51955-0.